

SUPER-EDDINGTON ACCRETION IN THE *WISE*-SELECTED EXTREMELY LUMINOUS INFRARED GALAXY W2246–0526

CHAO-WEI TSAI¹, PETER R. M. EISENHARDT², HYUNSUNG D. JUN³, JINGWEN WU⁴,
ROBERTO J. ASSEF⁵, ANDREW W. BLAIN⁶, TANIO DIAZ-SANTOS⁵, SUZY F. JONES⁷,
DANIEL STERN², EDWARD L. WRIGHT¹, AND SHERRY C. C. YEH⁸

Accepted by the Astrophysical Journal

ABSTRACT

We use optical and near-infrared spectroscopy to observe rest-UV emission lines and estimate the black hole mass of WISEA J224607.56–052634.9 (W2246–0526) at $z = 4.601$, the most luminous hot dust-obscured galaxy yet discovered by *WISE*. From the broad component of the Mg II-2799Å emission line, we measure a black hole mass of $\log(M_{\text{BH}}/M_{\odot}) = 9.6 \pm 0.4$. The broad C IV-1549Å line is asymmetric and significantly blueshifted. The derived M_{BH} from the blueshift-corrected broad C IV line width agrees with the Mg II result. From direct measurement using a well-sampled SED, the bolometric luminosity is $3.6 \times 10^{14} L_{\odot}$. The corresponding Eddington ratio for W2246–0526 is $\lambda_{\text{Edd}} = L_{\text{AGN}}/L_{\text{Edd}} = 2.8$. This high Eddington ratio may reach the level where the luminosity is saturating due to photon trapping in the accretion flow, and be insensitive to the mass accretion rate. In this case, the M_{BH} growth rate in W2246–0526 would exceed the apparent accretion rate derived from the observed luminosity.

Keywords: Galaxies: individual: WISEA J224607.56–052634.9 – Galaxies: nuclei – Galaxies: active – Quasars: supermassive black holes – Quasars: emission lines – Infrared: galaxies

1. INTRODUCTION

Discovered by their unusual mid-infrared colors in the *Wide-field Infrared Survey Explorer* (*WISE*; Wright et al. 2010) all-sky survey, Hot Dust-Obscured Galaxy (Hot DOG; Eisenhardt et al. 2012; Wu et al. 2012) are hyperluminous infrared galaxies with a wide IR plateau and a steep drop in the far IR, suggesting a broader dust temperature distribution (Tsai et al. 2015), which we model in C.-W. Tsai et al., (in preparation). W2246–0526 is the most luminous Hot DOG yet identified. With $L_{\text{bol}} > 3 \times 10^{14} L_{\odot}$, it is well into the Extremely Luminous Infrared Galaxy (ELIRG, $> 10^{14} L_{\odot}$; Tsai et al. 2015) range, and among the few most luminous galaxies known thus far.

Its superlative luminosity is not the result of gravitational lensing (Tsai et al. 2015; Díaz-Santos et al. 2016). To account for a significant fraction of this luminosity via a starburst would require a star formation rate (SFR) $\gg 10^4 M_{\odot} \text{ yr}^{-1}$ (Tsai et al. 2015), but the cool gas and dust supplies needed for such an extraordinary SFR are not in evidence. Instead, the spectral energy distribution (SED) of W2246–0526 is dominated by hot dust

($T_{\text{dust}} > 450 \text{ K}$; Tsai et al. 2015), indicative of a dominant AGN. Direct evidence for an accreting supermassive black hole (SMBH) in this system comes from the broad C IV line in its spectrum (Díaz-Santos et al. 2018), which we discuss in further detail below. This makes an obscured AGN the most straightforward power source for W2246–0526, and we assume this is the case for the remainder of this paper.

Like W2246–0526, many hyperluminous Hot DOGs show AGN features in their spectra (P. R. M. Eisenhardt et al., in preparation). Recently, Wu et al. (2018) detected broad H α lines in all members of a sample of five hyperluminous Hot DOGs at $1.6 < z < 2.5$, finding black hole masses in the range $\log(M_{\text{BH}}/M_{\odot}) = 8.7 - 9.5$. Compared to quasars with similar black hole masses, these Hot DOGs have higher luminosities. The SMBHs in these Hot DOGs are accreting at a rate close to the Eddington limit, suggesting that Hot DOGs represent a transitional phase of high accretion between obscured and unobscured quasars (Wu et al. 2018).

Is W2246–0526 similar to its sibling Hot DOGs? Is its extreme luminosity due to sub-Eddington accretion onto an exceptionally massive SMBH, or to an exceptionally high Eddington ratio for a more typical SMBH mass (Assef et al. 2015; Tsai et al. 2015)? To answer these questions, the virial mass of the SMBH in W2246–0526 needs to be determined. Measuring SMBH mass from C IV profiles is challenging in comparison to Balmer lines, with large scatter (e.g. Netzer et al. 2007; Shen et al. 2011) and possible bias due to outflows (Gaskell 1982; Murray & Chiang 1997; Leighly 2004). Although the H α and H β lines are stronger and suffer less from Fe II emission blending, for sources at higher redshift ($z > 4$), such as W2246–0526, only the broad Mg II line is reliable and available from the ground.

In this paper, we report the detection of broad Mg II

¹ Department of Physics and Astronomy, UCLA, Los Angeles, CA 90095-1547, USA; [email: cwtsai@astro.ucla.edu]

² Jet Propulsion Laboratory, California Institute of Technology, Pasadena, CA 91109, USA

³ School of Physics, Korea Institute for Advanced Study, Seoul 02455, Korea

⁴ National Astronomical Observatories, Chinese Academy of Sciences, Beijing, 100012, China

⁵ Núcleo de Astronomía de la Facultad de Ingeniería y Ciencias, Universidad Diego Portales, Av. Ejército Libertador 441, Santiago, Chile

⁶ Department of Physics & Astronomy, University of Leicester, Leicester, LE1 7RH, UK

⁷ Department of Space, Earth and Environment, Chalmers University of Technology, Onsala Space Observatory, Sweden

⁸ W. M. Keck Observatory, Waimea, HI 96743, USA

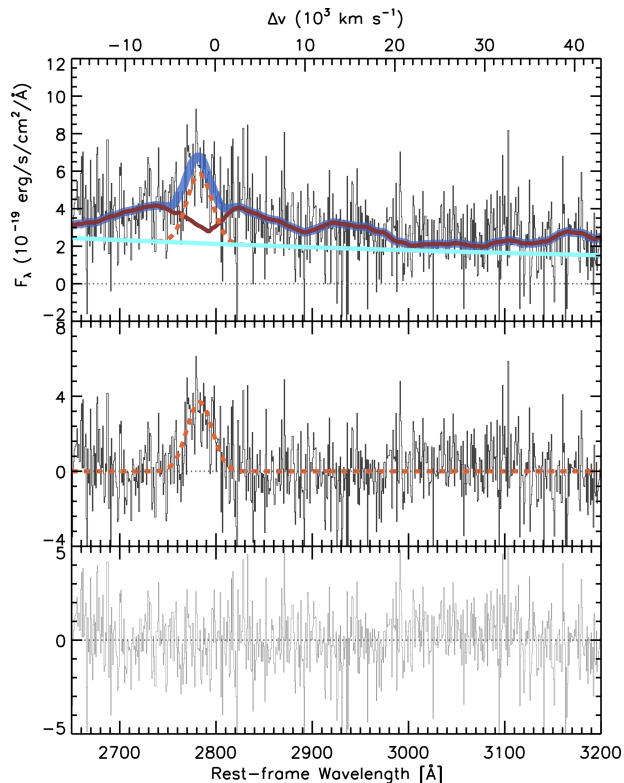


Figure 1. The observed near-IR spectrum of W2246–0526 around the Mg II 2799 Å emission line, with a model (blue solid line) containing a Gaussian profile for the Mg II line (orange dashed line), the Fe II complex (brown solid line), and a power-law continuum ($F_{\lambda} [10^{-19} \text{ erg s}^{-1} \text{ cm}^2 \text{ \AA}^{-1}] = 1.808 \times (\lambda/3000 \text{ \AA})^{-2.583}$, cyan solid line). Velocities are shown with respect to the [C II] redshift $z = 4.601$. The middle panel shows the spectrum and Mg II line component (FWHM = $3300 \pm 600 \text{ km s}^{-1}$, blueshifted by $1600 \pm 300 \text{ km s}^{-1}$) after the continuum and Fe II complex are subtracted. The residual spectrum is plotted in the lower panel.

emission in W2246–0526. We provide black hole mass estimates from the Mg II and C IV lines. To better determine the Eddington ratio, we also re-examine the luminosity estimate of W2246–0526 with updated photometric data. We present our near-infrared spectroscopy of W2246–0526 in Section 2, together with a description of other data used in this paper. Section 3 gives the SED, luminosity, and line widths based on these data. Section 4 considers the resulting black hole mass and Eddington ratio. In Section 5, we summarize our work. A redshift $z = 4.593$ for W2246–0526 was reported by Tsai et al. (2015), determined from the overall Ly α line profile. However, the redshift was revised to $z = 4.601$ based on the [C II] 157.7 μm line emission (Díaz-Santos et al. 2016). We adopt $z = 4.601$ for W2246–0526, and a cosmology with $H_0 = 70 \text{ km s}^{-1} \text{ Mpc}^{-1}$, $\Omega_m = 0.3$, and $\Omega_{\Lambda} = 0.7$.

2. OBSERVATIONS AND DATA REDUCTION

2.1. Keck OSIRIS Observation of the Mg II Line

At $z = 4.601$, the Mg II-2799 Å line of W2246–0526 falls at $1.567 \mu\text{m}$ in the H band. W2246–0526 was observed with Keck I telescope on UT 2016 October 21 in the first half of the night using OSIRIS (Larkin et al. 2006) while the originally proposed instrument (MOS-FIRE) was being repaired. The weather was clear and the seeing was $\sim 0''.7$ over the observation. The spectra

Table 1
Fluxes of W2246–0526

Band	Wavelength	Flux Density	Reference
WFC3 F160W	1.537 μm	$6.1 \pm 0.2 \mu\text{Jy}$	D16
K-band	2.159 μm	$8.9 \pm 2.8 \mu\text{Jy}$	A15
IRAC band 1	3.6 μm	$38 \pm 2 \mu\text{Jy}$	G12
IRAC band 2	4.5 μm	$33 \pm 1 \mu\text{Jy}$	G12
WISE band 3	12 μm	$2.5 \pm 0.2 \text{ mJy}$	T15
WISE band 4	22 μm	$15.9 \pm 1.6 \text{ mJy}$	T15
PACS blue channel	70 μm	$37 \pm 3 \text{ mJy}$	T15
PACS red channel	160 μm	$142 \pm 16 \text{ mJy}$	T15 ^a
SPIRE 250 μm	250 μm	$107 \pm 8 \text{ mJy}$	T15 ^a
SPIRE 350 μm	350 μm	$81 \pm 12 \text{ mJy}$	T15
SCUBA2 450 μm	450 μm	$49 \pm 12 \text{ mJy}$	J14, T18
SPIRE 500 μm	500 μm	$44 \pm 15 \text{ mJy}$	T15
SCUBA2 850 μm	850 μm	$11 \pm 2 \text{ mJy}$	J14
ALMA 882 μm	882 μm	$7.4 \pm 0.4 \text{ mJy}$	D16 ^b
ALMA 1.2 mm	1190 μm	$4.8 \pm 1.9 \text{ mJy}$	D18 ^c

Note. — The reference code in the last column: A15: Assef et al. (2015); G12: Griffith et al. (2012); D16: Díaz-Santos et al. (2016); D18: Díaz-Santos et al. (2018); J14: Jones et al. (2014); T15: Tsai et al. (2015); T18: This work. ^a The *Herschel* PACS 160 μm and SPIRE 250 μm measurements are updated. See text for details. ^b Flux within $1''$ diameter aperture. ^c Sum of W2246–0526 and the extended emission.

were taken with the Hbb filter covering $1.473 - 1.803 \mu\text{m}$ at $0.5 \text{ nm channel}^{-1}$ resolution. With the 4×4 dithering used, the $1''.6 \times 6''.4$ field-of-view of the integrated field unit covered $2''.0 \times 10''.9$ with $0''.1 \text{ pixel}^{-1}$ at a position angle of 337° centered on W2246–0526. The final spectral resolution of ~ 2.5 spaxels yielded $R = \lambda/\Delta\lambda \lesssim 3400$. Atmospheric wavefront errors were partially corrected with Laser Guild Star Adaptive Optics (LGS-AO) and a $R = 18.3$ tip-tilt star $26''.8$ to the south-west of W2246–0526. The integration time for each individual frame was 900 s, and a total of 4 hours (16 frames) of on-source data was collected.

The OSIRIS data were reduced with the OSIRIS data reduction pipeline (DRP) v4.0.0. A custom procedure was used to remove the sky emission using pixels near the science target and frames adjacent in time. About 6% of the data at wavelengths with substantial sky line residual presents were clipped. The telluric correction was applied using both the G2V star HD 216516, and the A0V star HD 219833. The flux calibration was done using the G2V star. Including the uncertainties due to calibrator flux, aperture correction, and Strehl ratio, the overall uncertainty in the calibrated fluxes is estimated to be $\sim 20\%$. The wavelength was calibrated to values in vacuum. The final mosaic data cube was produced using the LGS offsets between frames. Using the 2MASS point source catalog (Skrutskie et al. 2006) and the WFC3 image in F160W from *HST* (Díaz-Santos et al. 2016), we registered the final science data cube with the uncertainty in absolute astrometry estimated to be $< 0''.1$.

Due to the LGS-AO, the spatial resolution was sufficient to resolve the continuum profile of W2246–0526, with an estimated extent of $0''.36 \times 0''.29$ at PA = 155° , consistent with the *HST* observations (Díaz-Santos et al. 2016). The Mg II emission line of W2246–0526 was extracted from the OSIRIS data cube using a $0''.3$ aperture. An aperture correction was applied to the flux scale of the Mg II spectrum to match the photometry from the *HST* F160W image. The extracted and flux corrected spectrum is shown in Figure 1.

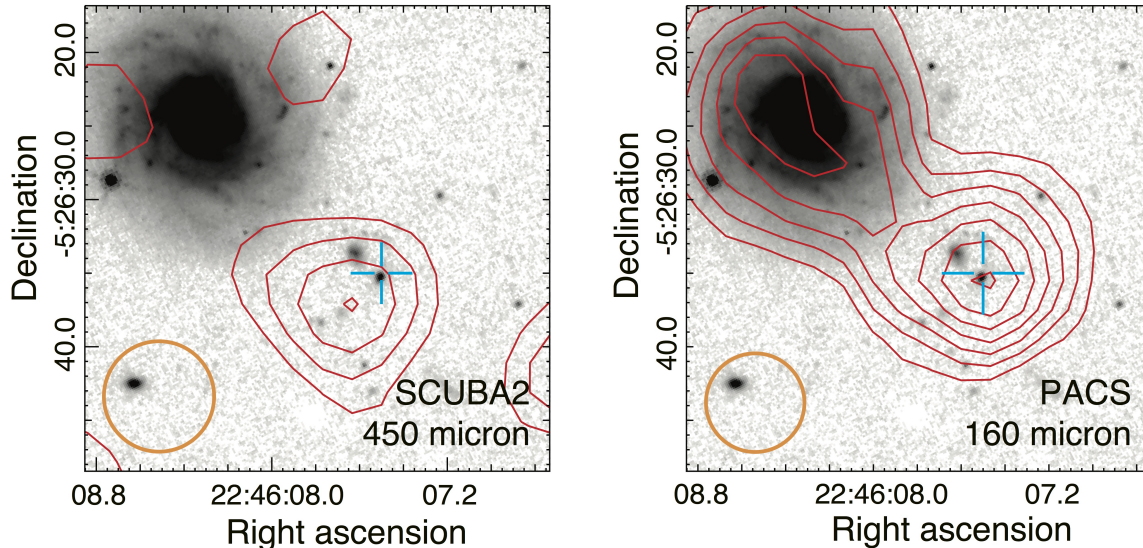


Figure 2. (*Left*) SCUBA2 450 μm contours at levels with an increment of 12 mJy beam^{-1} (1σ) and (*Right*) *Herschel* PACS 160 μm contours at levels of 30% – 100% by 10% steps overlaid on the *HST* F160W image of W2246–0526. The *WISE* position of the source is marked with the blue crosshair. The FWHM of the PACS 160 μm PSF is $6''.3$ and the beam size at 450 μm is $7''.5$, as shown at the lower right corners of the corresponding panels (orange). The peak of the 450 μm emission is marginally offset to the south-east of the *WISE* position by $2''.4 \pm 2''.2$. The foreground galaxy to the north-east at $z_{\text{phot}} = 0.047$ shows no significant detection at 450 μm , and is unlikely to significantly contaminate *Herschel* photometry at 250 μm –500 μm .

2.2. Other Data

For comparison to the SMBH mass estimate from Mg II we analyze an optical spectrum of the C IV line. To calculate the Eddington ratio, we estimate the luminosity using the observed spectral energy distribution (SED) of W2246–0526 from optical to submillimeter wavelengths. The flux densities and the references are listed in Table 1. These observations are described below.

2.2.1. Keck LRIS Observation of the C IV Line

As reported in Díaz-Santos et al. (2018), a one hour exposure optical spectrum of W2246–0526 was obtained on UT 2013 October 5 using LRIS (Oke et al. 1995) on the Keck I telescope, with spectral resolution ~ 750 and a $1''.5$ slit. Additional details of the observation are reported in Díaz-Santos et al. (2018).

2.2.2. SCUBA2 450 μm Observation

SCUBA2 observations with the JCMT, as reported by Jones et al. (2014), were obtained on UT 2012 May 23 and 26. During the 450 μm observations, the CSO 225 GHz sky opacity was $\tau_{225} \sim 0.05$, and the corresponding optical depth at 450 μm was $\tau_{450\mu\text{m}} \sim 1$. However, the two sets of observations identify a point source with a consistent flux density (within 1σ), slightly offset to the southeast from the *WISE* infrared position of W2246–0526. The position offset ($2''.4 \pm 2''.2$) is consistent with the pointing uncertainty during the observation. The total time per source was 120 min using the CV DAISY mode, providing deep coverage in the central $3'$ diameter region. The final map that combines both sets of observations is shown in the left panel of Figure 2.

2.2.3. *Herschel* Observations

Herschel fluxes for W2246–0526 were reported in Tsai et al. (2015). There is a foreground spiral galaxy (SDSS J224608.38–052624.3; Csabai et al. 2003; Beck et al. 2016, photometric redshift 0.047 ± 0.024) $\sim 16''.5$ to the north-east of W2246–0526, with $r_{\text{PETRO}} = 8''.3$ (Figure 2). With the $\sim 12''$ FWHM beam size for PACS at 160 μm this could affect the *Herschel* fluxes of W2246–0526 reported in Tsai et al. (2015). For the SPIRE bands, the larger beam size ($18''$ to $37''$) increases the possibility of flux contamination. This concern has been raised by Fan et al. (2018), who have tried to estimate the contribution of the foreground galaxy to the *Herschel* photometry with PSF fitting and SED modeling. However, the estimated flux contamination in that work does not reconcile with the results of the *Herschel*/PACS Point Source Catalogue (Marton et al. 2017), in which both the foreground galaxy and W2246–0526 are detected using PSF photometry. We remeasured the 160 μm flux density of W2246–0526 excluding emission from the extended profile of the foreground galaxy by using an irregular polygon aperture, finding $F_{160\mu\text{m}} \sim 142$ mJy, 25% less than reported in Tsai et al. (2015). All other *Herschel* photometry in Tsai et al. (2015) agrees with the results from the *Herschel*/PACS Point Source Catalogue (Marton et al. 2017) and *Herschel*/SPIRE Point Source Catalogue (SPSC; Schulz et al. 2017) within 1σ , except the flux density for SPIRE at 250 μm which is $\sim 2\sigma$ lower than the SPSC value. For consistency, we adopt the SPSC flux at 250 μm . We note that the SPIRE maps all show a point source with the peak within the corresponding FWHM from W2246–0526. Our ground-based JCMT SCUBA2 maps at 450 μm and 850 μm , with beam sizes of $7''.5$ and $15''$, also show that the observed submillimeter emission is concentrated at W2246–0526 (Jones et al. 2014) with no significant emission detected around the foreground galaxy (see Figure 2–left). W2246–0526

dominates the observed far-IR and submillimeter emission over the adjacent spiral galaxy. Using the peak flux at the pixel of the foreground galaxy center, we estimate the SPIRE band photometry contamination by the foreground source is $< 30\%$. From the ALMA 252 GHz continuum map with a $20''.2$ half-power-beam-width primary beam (Díaz-Santos et al. 2018), the dust emission from the foreground galaxy is $< 10\%$ of the flux of W2246–0526 system at 1.2 mm.

3. ANALYSIS

3.1. SED and Luminosity

The SED of W2246–0526 is shown in Figure 3, based on the updated photometric data listed in Table 1. Unlike optical QSOs in which a large fraction of energy escapes at UV wavelengths, most of the energy from W2246–0526 is seen at rest-frame infrared wavelengths ($> 1 \mu\text{m}$). The broad Mg II and C IV emission lines observed in W2246–0526 provide direct evidence for the presence of an AGN, and the infrared emission most plausibly arises from hot dust obscuring the AGN. The rest-frame UV and optical continuum emission, which are assumed to be primarily from the host galaxy of the obscured AGN, contribute $\lesssim 1\%$ of the total luminosity. Like other Hot DOGs, the infrared SED of W2246–0526 shows this plateau, but, interestingly, also shows a dip with respect to other Hot DOGs at rest-frame $\sim 12.5 \mu\text{m}$ ($70 \mu\text{m}$ in the observed frame). This prompts us to suggest that silicate absorption may be affecting the SED.

At $z = 4.601$, the broad $9.7 \mu\text{m}$ silicate absorption feature overlaps with the 60 - $85 \mu\text{m}$ bandpass of the PACS $70 \mu\text{m}$ filter, and can account for the dip in the SED if the strength of the absorption in W2246–0526 is comparable to that in the heavily enshrouded nucleus of NGC 4418 (Roche et al. 1986; Spoon et al. 2001), the ULIRG Arp 220 (Polletta et al. 2007), or the HyLIRG IRAS 08572+3915 (Spoon et al. 2007; Vega et al. 2008; Efstathiou et al. 2014). In Figure 3, we plot a template of the silicate absorption in NGC 4418 scaled to match the observed $70 \mu\text{m}$ photometry (for clarity we omit showing the relatively weak $9.66 \mu\text{m}$ H₂ 0–0 S(3) emission line).

We find the bolometric luminosity of W2246–0526 is $L_{\text{bol}} = 3.6 \pm 0.3 \times 10^{14} L_{\odot}$, using the observed flux density measurements listed in Table 1. This estimate follows the methodology of Tsai et al. (2015) by integrating a power law interpolated between photometric data. We assume essentially all of this luminosity comes from a quasar shrouded within a dust cocoon.

Hot dust emission dominates the energy output, as indicated by the SED. Because of the high luminosity, the dust sublimation radius is ~ 15 pc for W2246–0526 (Barvainis 1987; Tsai et al. 2015), substantially larger than the radius of the broad line region (~ 1.3 pc, based on Bentz et al. 2009). Thus the thermal dust emission can not vary dramatically within the light-crossing rest-frame timescale of ~ 50 yr, or ~ 280 yr in the observed frame. This timescale is even longer for the dust emission at the longer wavelengths of the SED plateau. Therefore we do not anticipate observable variability in the bolometric luminosity of W2246–0526.

3.2. Mg II Emission Line Width

The observed Mg II 2799Å emission line and the line model are shown in Figure 1, which covers the spectrum

at rest-frame wavelengths between 2630Å – 3220Å . The signal-to-noise ratio of the continuum and the Mg II line (within FWHM from the line center) are 1.4 and 7.7 per spectral element (0.82Å , rest), respectively.

The Mg II doublet line profile was fit after modeling the blended Fe II line complex and a power-law continuum. The profile of the Fe II complex used templates from (Tsuzuki et al. 2006). Least-squares model fitting was done using the Levenberg-Marquardt algorithm as implemented in IDL MPFIT (Markwardt 2009). Excluding the Mg II region, we stepped through a grid of Fe II widths with FWHM=0 to 18000 km s^{-1} and a 600 km s^{-1} step size, finding the best fit continuum (given in the Figure 1 caption) and Fe II model strength. We then fit the residual with a single Gaussian model for the Mg II line, iterating up to 20 times until the parameters stay unchanged to floating point precision.

Although the signal-to-noise ratios are not high, they do not significantly affect the reliability for the line profile measurements, because of the broad line width. The best-fit model yields a Gaussian with a FWHM of $3300 \pm 600 \text{ km s}^{-1}$, and a blueshifted velocity offset of $\Delta v = 1600 \pm 300 \text{ km s}^{-1}$ with respect to the [C II] redshift (Díaz-Santos et al. 2016).

3.3. C IV Emission Line Width

At $z = 4.601$, the C IV line shifts to $\sim 8674 \text{Å}$. As noted in Díaz-Santos et al. (2018), the C IV line in W2246–0526 is highly asymmetric, broad, and significantly blue-shifted relative to this ALMA-derived [C II] redshift. Following a similar approach to that used by Shen et al. (2008, 2011) and Jun et al. (2017), we model the C IV line of W2246–0526 with two components as shown in Figure 4. The signal-to-noise ratio of the continuum and the C IV line are 4.2 and 13.4 per spectral element (2.1Å , rest), respectively.

As we did for Mg II, we first solved for a power-law continuum (given in the Figure 4 caption) and the Fe II line complex (using the template from Vestergaard & Wilkes 2001), as well as the He II- 1640Å line. The strength of the Fe II complex was matched to that of the Fe II around the Mg II region using overlapping wavelengths in the templates, and the Fe II line widths were set to be identical for the Mg II and C IV regions.

The narrower Gaussian component has a FWHM = $1600 \pm 140 \text{ km s}^{-1}$, blueshifted by $3000 \pm 80 \text{ km s}^{-1}$ with respect to the system redshift, while the broader component has FWHM = $9000 \pm 140 \text{ km s}^{-1}$ and is blueshifted by $3420 \pm 70 \text{ km s}^{-1}$. The composite double-Gaussian profile has FWHM = $5900 \pm 100 \text{ km s}^{-1}$ and a blueshift of $3300 \pm 70 \text{ km s}^{-1}$. This blueshift of the C IV line profile in W2246–0526 is significantly higher than the median blueshift observed in SDSS QSOs (median = 890 km s^{-1} for 492 quasars at $4.5 < z < 4.7$; Shen et al. 2011), and more comparable to the median blueshift of 2520 km s^{-1} for 9 quasars at $z \gtrsim 6.4$ that have C IV emission line measurements (Mazzucchelli et al. 2017).

4. RESULTS AND DISCUSSION

4.1. Mg II-based SMBH Mass

Masses of the SMBH in AGNs are usually determined from the measurements of broad emission lines, assuming virialized gas motion. This approach was established

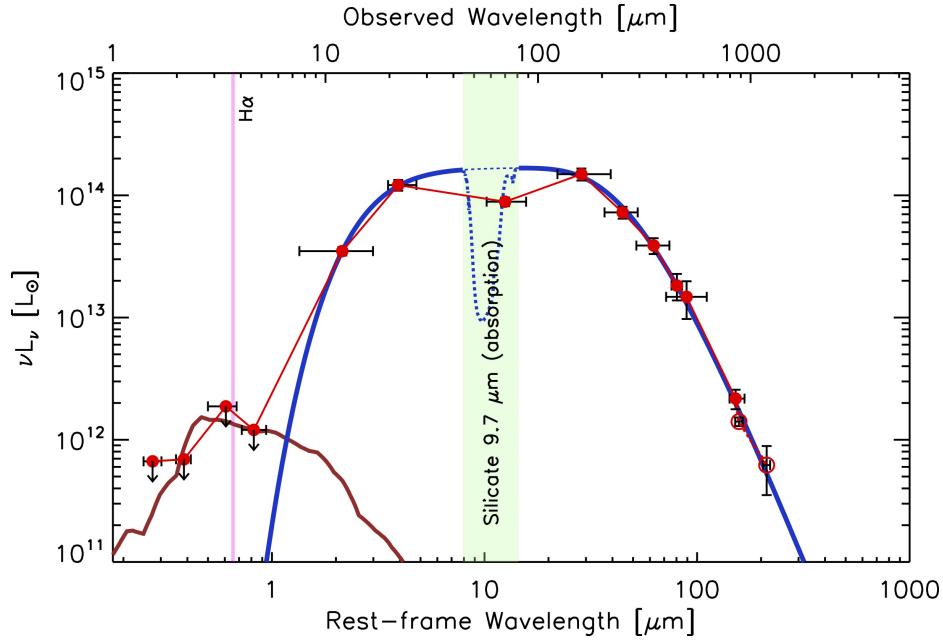


Figure 3. SED of W2246–0526. The filled red points represent photometric measurements with detections ($> 3\sigma$). The two open red circles are the integrated flux from ALMA measurements of the resolved emission. The downward arrows at rest-frame wavelengths shorter than $1 \mu\text{m}$ indicate that these data are only used as upper limits in the SED fitting. The light green shaded area indicates the wavelength range of a broad silicate absorption feature which could be the cause of the PACS $70 \mu\text{m}$ flux deficit. The blue line shows an SED model with a continuous dust temperature distribution (C.-W. Tsai et al., in preparation) with an empirical silicate absorption feature template scaled to match the photometry (dotted blue line). The magenta line marks the wavelength of the $\text{H}\alpha$ line. The brown solid line represents the SED of a 1.3 Gyr-old elliptical galaxy with a total stellar mass of $1.1 \times 10^{12} M_{\odot}$ generated with the GRASIL code.

via variability monitoring (reverberation mapping; see e.g. Peterson 1993) and subsequently calibrated to single epoch measurements of the $\text{H}\beta$ line width and 5100 \AA continuum (e.g. Wandel et al. 1999; Kaspi et al. 2000; Vestergaard 2002), and extended to other line widths. For objects at $z > 1$, the $\text{H}\beta$ line is redshifted into the infrared, stimulating the use of the broad Mg II line from optical spectroscopy for SMBH mass determination (McLure & Jarvis 2002; Onken & Kollmeier 2008; Trakhtenbrot & Netzer 2012; Marziani et al. 2013). Advances in near-IR instrumentation have made near-IR spectroscopy of distant objects feasible, enabling the Balmer lines to be used for SMBH measurement to $z \sim 2.5\text{--}3.5$ (e.g. Wu et al. 2018). At $z > 3.5$ the Mg II line is also observed at $> 1 \mu\text{m}$, and Mg II is usually used for black hole mass (M_{BH}) measurement of objects at the highest redshifts (Wu et al. 2015; Bañados et al. 2018). The calibration of Mg II -determined SMBH masses with respect to those from $\text{H}\beta$ has been established (McLure & Dunlop 2004; Wang et al. 2009; Shen et al. 2011; Jun et al. 2015; Suh et al. 2015). In this paper, we adopt the Mg II -based SMBH mass formulation from Equation 10 of Wang et al. (2009):

$$\log\left(\frac{M_{\text{BH}}}{M_{\odot}}\right) = (7.13 \pm 0.27) + 0.5 \log\left(\frac{L_{3000}}{10^{44} \text{ erg s}^{-1}}\right) + (1.51 \pm 0.49) \log\left(\frac{\text{FWHM}_{\text{Mg II}}}{1000 \text{ km s}^{-1}}\right), \quad (1)$$

where L_{3000} is the monochromatic luminosity at rest-frame 3000 \AA , and $\text{FWHM}_{\text{Mg II}}$ is the full-width-half-maximum of the Mg II line profile (given in section 3.2).

Because of the high extinction in W2246–0526, esti-

mates of L_{3000} from the rest-UV continuum are uncertain. Instead, we use $L_{3000} \sim 0.19 \times L_{\text{bol}}$ based on the empirical unobscured AGN SED model of Richards et al. (2006). For $L_{\text{bol}} = 3.6 \times 10^{14} L_{\odot}$, $L_{3000} = 2.6 \times 10^{47} \text{ erg s}^{-1}$. The observed rest-frame 3000 \AA continuum flux in W2246–0526 is only about 0.02 of the anticipated value from this template. With the Mg II FWHM of $3300 \pm 600 \text{ km s}^{-1}$, this yields $\log(M_{\text{BH}}/M_{\odot}) = 9.6 \pm 0.4$. The error range includes the 1σ systematic uncertainties from Equation 1 and from the Mg II profile fitting. The statistical uncertainty of M_{BH} due to the Mg II line width uncertainty is 0.05 dex.

The Richards et al. (2006) SED model assumes the emission from a quasar is isotropic. However, the unobscured quasars used to construct the SED presumably have a surrounding dusty torus with a low inclination and a covering factor that intercepts and reprocesses some of the quasar emission, so that it appears again in the IR. Thus the L_{bol} from the SED model would be overestimated by $(1 + CF_{\text{u}})$ where CF_{u} is the covering factor for the unobscured quasars used in Richards et al. (2006), and L_{3000} would represent a larger portion of the true L_{bol} . For W2246–0526 which has a well determined L_{bol} , this suggests using a ratio of L_{3000}/L_{bol} which is $(1 + CF_{\text{u}})$ larger. The covering factor cannot be higher than 1 (especially for an unobscured quasar sample), so using Equation 1, this correction would increase $\log(M_{\text{BH}}/M_{\odot})$ by < 0.15 . Both of these terms are smaller than other estimates of the overall systematic uncertainty, which are up to 0.3 dex (Denney et al. 2009; Wang et al. 2009; Jun et al. 2015).

4.2. CIV-based M_{BH} Estimate

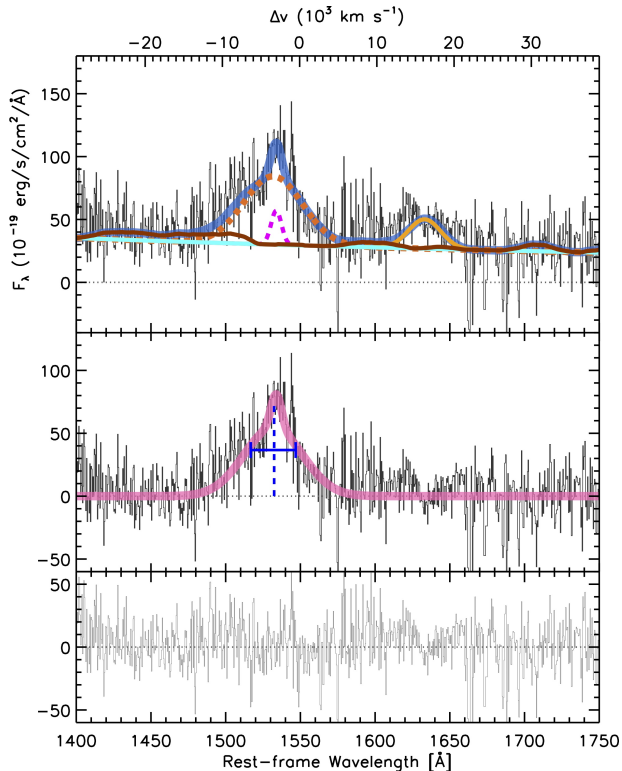


Figure 4. The observed optical (rest UV) spectrum of W2246–0526 is shown in the top panel, with a model (blue solid line) containing two independent Gaussian C IV-1488,1551 Å emission line profiles (orange and magenta dashed lines), the He II-1640 Å line (orange solid line), the Fe II line complex (brown solid line), and a power-law continuum ($F_{\lambda} [10^{-19} \text{ erg s}^{-1} \text{ cm}^{-2} \text{ \AA}^{-1}] = 38.00 \times (\lambda/1350 \text{ \AA})^{-1.784}$; cyan solid line). Velocities are shown with respect to the [C II] redshift of $z = 4.601$. The middle panel shows the composite of the two Gaussian models ($\text{FWHM} = 5900 \pm 100 \text{ km s}^{-1}$, blueshifted by $3300 \pm 70 \text{ km s}^{-1}$) overlaid on the observed spectrum after subtracting the other model components. The residual spectrum is presented in the lower panel.

The C IV line profiles of AGNs often show an enhanced blue wing, significantly different from their $H\beta$ line profiles. This highlights the issue of the virial assumption for C IV, and results in a large and biased offset when comparing C IV-based M_{BH} estimates to those based on $H\beta$ and Mg II (Netzer et al. 2007; Shen et al. 2011). In addition, the broad C IV-1549 Å feature is often substantially blueshifted with respect to the system rest frame (e.g. Richards et al. 2002), especially for high luminosity objects (Baskin & Laor 2005). The blueshift is usually attributed to the wind component of the broad line region, or outflow (Gaskell 1982; Murray & Chiang 1997; Leighly 2004). Nevertheless, because of the accessibility of the C IV line from the ground for the quasars over a large range of redshift ($1.3 \lesssim z \lesssim 5$), efforts have been made to calibrate C IV-based M_{BH} estimates to $H\beta$ -based values in Type-1 AGNs (Vestergaard & Peterson 2006; Assef et al. 2011; Shen et al. 2011; Denney 2012; Denney et al. 2013; Runnoe et al. 2013; Park et al. 2017) although C IV is not considered as reliable as Mg II (Fine et al. 2010; Jun et al. 2015; Mejía-Restrepo et al. 2016). Motivated by the significance of the C IV asymmetry in a principal component analysis of AGNs (Sulentic et al. 2007), a simple correction to the C IV-based M_{BH} es-

timate has recently been suggested (Brotherton et al. 2015; Coatman et al. 2016, 2017; Jun et al. 2017). This correction calibrates the FWHM of the C IV line to the expected virial C IV FWHM from the Balmer line widths using the C IV blueshift.

As noted in section 3.3, the C IV line in W2246–0526 is highly asymmetric, broad, and significantly blue-shifted relative to the [C II] redshift. Using the composite Gaussian model and adopting the correction of Coatman et al. (2017):

$$\text{FWHM}_{\text{CIV}}^{\text{Corr.}} = \frac{\text{FWHM}_{\text{CIV}}^{\text{Measured}}}{(0.36 \pm 0.03) \left(\frac{\text{CIV}_{\text{blueshift}}}{10^3 \text{ km s}^{-1}}\right) + (0.61 \pm 0.04)}, \quad (2)$$

we obtain a corrected FWHM for the broad C IV component of $\text{FWHM}_{\text{CIV}}^{\text{Corr.}} = 3300 \pm 400 \text{ km s}^{-1}$, a factor 1.8 smaller than the FWHM derived from our two component analysis.

To estimate the black hole mass, we adopt the methodology of Coatman et al. (2017):

$$\log\left(\frac{M_{\text{BH}}}{M_{\odot}}\right) = 6.71 + 2 \log\left(\frac{\text{FWHM}_{\text{CIV}}^{\text{Corr.}}}{10^3 \text{ km s}^{-1}}\right) + 0.53 \log\left(\frac{L_{1350}}{10^{44} \text{ erg s}^{-1}}\right). \quad (3)$$

L_{1350} is the monochromatic luminosity at 1350 Å, and is estimated to be $L_{1350} \sim 0.26 \times L_{\text{bol}} = 3.6 \times 10^{47} \text{ erg s}^{-1}$ using the AGN template of Richards et al. (2006).

Using the corrected value for the broad C IV component, this yields $\log(M_{\text{BH}}/M_{\odot}) = 9.6 \pm 0.4$ including systematic uncertainty, nearly identical to the M_{BH} estimated using the Mg II line. The agreement of the M_{BH} estimate using the C IV line profile with that from the Mg II line measurement may be coincidental. It has been argued that a large component of the broad C IV emission line is observed to not reverberate for nearby AGNs based on reverberation mapping studies (e.g., Denney 2012).

4.3. $M_{\text{BH}}-M_{\text{sph}}$ Relation

From a sample of five Hot DOGs with M_{BH} measurements, Wu et al. (2018) found that the ratio of M_{BH} to the stellar mass in the spheroidal component of the host galaxy ($M_{\text{BH}}-M_{\text{sph}}$) in these systems is closer to the $M_{\text{BH}}-M_{\text{sph}}$ relation seen in local active galaxies (Bennert et al. 2011) than are the ratios seen in $z \sim 1.3$ quasars.

We estimate the bulge mass in W2246–0526 from K and $4.5 \mu\text{m}$ photometry using the synthesized elliptical galaxy SED template from the GRASIL code (Silva et al. 1998) to represent the spheroidal component, omitting the $3.6 \mu\text{m}$ data point which may be significantly elevated by $H\alpha$ emission line (see Figure 3). In Figure 3, the brown solid line shows the SED of an elliptical galaxy at an age of 1.3 Gyr with $M_{\text{sph}} = 1.1 \times 10^{12} M_{\odot}$. This can be considered as an upper limit of bulge mass of W2246–0526. This value is similar to the $\log(M_{\text{sph}}/M_{\odot}) = 11.9$ value expected from the local $M_{\text{BH}}-M_{\text{sph}}$ relation (Bennert et al. 2011):

$$\log(M_{\text{BH}}/M_{\odot}) = -3.34 \pm 1.91 + (1.09 \pm 0.18) \times \log(M_{\text{sph}}/M_{\odot}). \quad (4)$$

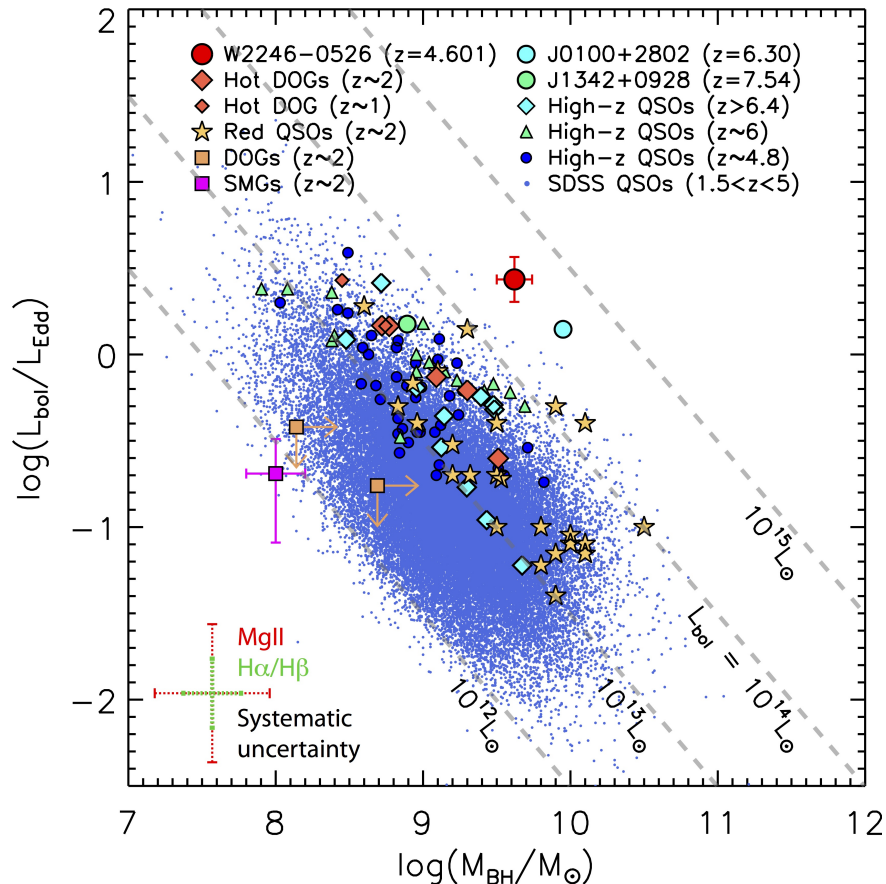


Figure 5. Eddington ratio vs BH mass for unobscured and obscured quasars including W2246–0526, following Wu et al. (2018). The plotted data include W2246–0526 (this work), J0100+2802 (Wu et al. 2015), J1342+0928 (Bañados et al. 2018), QSOs at $z \gtrsim 6.4$ (Mazzucchelli et al. 2017), QSOs at $z \sim 6$ (Wang et al. 2010; De Rosa et al. 2011), QSOs at $z \sim 4.8$ (Trakhtenbrot et al. 2011), SDSS QSOs at $1.5 < z < 5$ (Shen et al. 2011), Hot DOGs at $z \sim 2$ (Wu et al. 2018), Hot DOG at $z \sim 1$ (Ricci et al. 2017), red QSOs (Banerji et al. 2012, 2015), DOGs (Melbourne et al. 2011, 2012), and SMGs (Alexander et al. 2008). Typical systematic uncertainties are shown by the error bars plotted at the lower left, with the errors for the broad Mg II line estimates in red and the errors for the broad Balmer line estimates in green.

This suggests that W2246–0526 has a similar $M_{\text{BH}}-M_{\text{sph}}$ relation to the Hot DOGs shown in Figure 9 of Wu et al. (2018).

4.4. Eddington Ratio and Black Hole Accretion

In Wu et al. (2018), we argue that Hot DOGs are on the high luminosity tail for a given M_{BH} with respect to SDSS QSOs because they achieve the highest accretion rates, implying that they are accreting material at the highest rates possible. To illustrate this, in Figure 5, we plot Eddington ratio ($\lambda_{\text{Edd}} \equiv L_{\text{AGN}}/L_{\text{Edd}}$) vs. M_{BH} . With $\log(M_{\text{BH}}/M_{\odot}) = 9.6 \pm 0.4$, and $\log(L_{\text{bol}}/L_{\odot}) = 14.6$, the Eddington ratio of W2246–0526 is $\lambda_{\text{Edd}} = 2.8^{+0.9}_{-0.7}$ (statistical uncertainty), the highest of all the Hot DOGs for which we have so far obtained M_{BH} measurements (Wu et al. 2018), and putting the SMBH of W2246–0526 well into the super-Eddington accretion region. The total uncertainty for the λ_{Edd} , as shown by the dotted error bars in Figure 5 for W2246–0526, is 0.4 dex, dominated by the systematic uncertainty of M_{BH} . This systematic uncertainty also applies to the all objects at $z > 4$ in Figure 5.

Eddington ratios this large may attain a saturation level suggested by theoretical models (Wang & Zhou 1999; Watarai et al. 2000; Mineshige et al. 2000). At

high accretion rates, radiation pressure may dominate the accretion flow geometry, making the accretion disk “slim” (Abramowicz et al. 1988). In these models, the fast radial transportation of mass in the accretion flow geometry can trap most photons, preventing them from escaping, and carrying them inward to the SMBH. This photon trapping accretion makes the radiation efficiency inversely proportional to the mass accretion rate. As a result, the luminosity of a super-Eddington accreting black hole may reach saturation at an apparent Eddington ratio of $\lambda_{\text{Edd}} \sim 2$. The bolometric luminosity will increase much more slowly than the accretion rate, and the M_{BH} can increase much faster than the growth rate under the Eddington limit. In this scenario, the actual accretion rate of W2246–0526 may be higher than the observed λ_{Edd} suggests.

Although they have similarly high luminosities, as shown in Figure 5, the λ_{Edd} of W2246–0526 may have reached saturation while the QSO J0100+2802 has not. The difference in the λ_{Edd} of the sources is significant, considering only the statistical uncertainties from the measurements, but may not be when including systematic uncertainties in the M_{BH} estimate. We speculate that the difference between the sources, if real, is due to the much higher obscuration (thus more material to

accrete) in W2246–0526 or due to a different accreting geometry such as mass inflow from merging events. In this context, it is intriguing to note that recent ALMA observations of W2246–0526 of dust continuum emission at rest $212\mu\text{m}$ reveal bridges of dusty, metal-enriched material connecting three companions to the central galaxy (Díaz-Santos et al. 2018), implying that a multiple merger is in progress. Díaz-Santos et al. (2018) estimate that accretion rates of as high as $\dot{M} \sim 900 M_{\odot} \text{ yr}^{-1}$ onto the central core of W2246–0526 could be underway - sufficient to power the high luminosity of W2246–0526 which has a BH accretion rate of $24 M_{\odot} \text{ yr}^{-1}$ if a radiation efficiency of 0.1 is assumed.

5. CONCLUSION

We report observations of broad Mg II and C IV lines in the $z = 4.601$ source W2246–0526, the most luminous galaxy known, providing clear evidence for the presence of an AGN in the system. The FWHM of Mg II is 3300 km s^{-1} . Using the well-determined bolometric luminosity and an AGN template to estimate the 3000 \AA continuum luminosity, we measure the black hole mass $\log(M_{\text{BH}}/M_{\odot}) = 9.6 \pm 0.4$. The broad (5900 km s^{-1}) C IV line is significantly blueshifted, (by 3300 km s^{-1}), and we estimate the corresponding M_{BH} for this line using an empirically calibrated correction for the FWHM based on the blueshift. This method yields $\log(M_{\text{BH}}/M_{\odot}) = 9.6 \pm 0.4$, in good agreement with the Mg II estimate.

We reevaluate the bolometric luminosity of W2246–0526 considering the possible contribution of a nearby foreground galaxy. SCUBA2 $450 \mu\text{m}$ observations show that W2246–0526 dominates the far-IR flux. Using an ALMA 252 GHz continuum map, we estimate the contribution from the foreground galaxy is $<10\%$. The updated estimate of L_{bol} , based on power-law interpolation of the well sampled SED, is $3.6 \times 10^{14} L_{\odot}$. The SED shows a dip near rest $10\mu\text{m}$ suggestive of silicate absorption.

The Eddington ratio in W2246–0526 is 2.8. Theoretical arguments suggest the luminosity may be saturating in this super-Eddington regime, and be insensitive to the mass accretion rate. In this scenario, the M_{BH} growth rate may hence exceed the apparent accretion rate derived from the observed luminosity.

The authors gratefully acknowledge the anonymous referee for valuable comments and suggestions that improved the paper. C.-W.T. would like to thank Jian-Min Wang for the valuable discussions. This material is based upon work supported by the National Aeronautics and Space Administration under Proposal No. 13-ADAP13-0092 issued through the Astrophysics Data Analysis Program. H.D.J. is supported by Basic Science Research Program through the National Research Foundation of Korea (NRF) funded by the Ministry of Education (NRF-2017R1A6A3A04005158). J.W. is supported by the National Key Program for Science and Technology Research and Development of China (grant 2016YFA0400702) and Project 11673029 supported by NSFC. RJA was supported by FONDECYT grant number 1151408. T.D.-S. acknowledges support from ALMA-CONICYT project 31130005 and FONDECYT regular project 1151239. This publication makes use of data ob-

tained at the W.M. Keck Observatory, which is operated as a scientific partnership among Caltech, the University of California and NASA. The Keck Observatory was made possible by the generous financial support of the W.M. Keck Foundation. The authors wish to recognize and acknowledge the very significant cultural role and reverence that the summit of Mauna Kea has always had within the indigenous Hawaiian community. We are most fortunate to have the opportunity to conduct observations from this mountain. This publication makes use of data products from the *Wide-field Infrared Survey Explorer*, which is a joint project of the University of California, Los Angeles, and the Jet Propulsion Laboratory, California Institute of Technology, funded by the National Aeronautics and Space Administration. This research has made use of the NASA/IPAC Infrared Science Archive, which is operated by the Jet Propulsion Laboratory, California Institute of Technology, under contract with the National Aeronautics and Space Administration.

Facilities: Keck:I (OSIRIS, LRIS), Herschel Space Telescope, Wide-field Infrared Survey Explorer, JCMT

REFERENCES

- Abramowicz, M. A., Czerny, B., Lasota, J. P., & Szuszkiewicz, E. 1988, *ApJ*, 332, 646
- Alexander, D. M., Brandt, W. N., Smail, I., et al. 2008, *AJ*, 135, 1968
- Assef, R. J., Denney, K. D., Kochanek, C. S., et al. 2011, *ApJ*, 742, 93
- Assef, R. J., Eisenhardt, P. R. M., Stern, D., et al. 2015, *ApJ*, 804, 27
- Banerji, M., McMahon, R. G., Hewett, P. C., et al. 2012, *MNRAS*, 427, 2275
- Banerji, M., Alaghband-Zadeh, S., Hewett, P. C., & McMahon, R. G. 2015, *MNRAS*, 447, 3368
- Bañados, E., Venemans, B. P., Mazzucchelli, C., et al. 2018, *Nature*, 553, 473
- Barvainis, R. 1987, *ApJ*, 320, 537
- Baskin, A., & Laor, A. 2005, *MNRAS*, 356, 1029
- Beck, R., Dobos, L., Budavári, T., Szalay, A. S., & Csabai, I. 2016, *MNRAS*, 460, 1371
- Bennert, V. N., Auger, M. W., Treu, T., Woo, J.-H., & Malkan, M. A. 2011, *ApJ*, 726, 59
- Bentz, M. C., Peterson, B. M., Netzer, H., Pogge, R. W., & Vestergaard, M. 2009, *ApJ*, 697, 160
- Brotherton, M. S., Runnoe, J. C., Shang, Z., & DiPompeo, M. A. 2015, *MNRAS*, 451, 1290
- Coatman, L., Hewett, P. C., Banerji, M., & Richards, G. T. 2016, *MNRAS*, 461, 647
- Coatman, L., Hewett, P. C., Banerji, M., et al. 2017, *MNRAS*, 465, 2120
- Csabai, I., Budavári, T., Connolly, A. J., et al. 2003, *AJ*, 125, 580
- Denney, K. D., Peterson, B. M., Dietrich, M., Vestergaard, M., & Bentz, M. C. 2009, *ApJ*, 692, 246
- Denney, K. D., Pogge, R. W., Assef, R. J., et al. 2013, *ApJ*, 775, 60
- Denney, K. D. 2012, *ApJ*, 759, 44
- De Rosa, G., Decarli, R., Walter, F., et al. 2011, *ApJ*, 739, 56
- Díaz-Santos, T., Assef, R. J., Blain, A. W., et al. 2018, *Science*, submitted
- Díaz-Santos, T., Assef, R. J., Blain, A. W., et al. 2016, *ApJ*, 816, L6
- Efstathiou, A., Pearson, C., Farrah, D., et al. 2014, *MNRAS*, 437, L16
- Eisenhardt, P. R. M., Wu, J., Tsai, C.-W., et al. 2012, *ApJ*, 755, 173
- Eisenhardt, P. R. M., et al., in preparation
- Fan, L., Gao, Y., Knudsen, K. K., & Shu, X. 2018, *ApJ*, 854, 157

- Fine, S., Croom, S. M., Bland-Hawthorn, J., et al. 2010, *MNRAS*, 409, 591
- Gaskell, C. M. 1982, *ApJ*, 263, 79
- Griffith, R. L., Kirkpatrick, J. D., Eisenhardt, P. R. M., et al. 2012, *AJ*, 144, 148
- Jones, S. F., Blain, A. W., Stern, D., et al. 2014, *MNRAS*, 443, 146
- Jun, H. D., Im, M., Lee, H. M., et al. 2015, *ApJ*, 806, 109
- Jun, H. D., Im, M., Kim, D., & Stern, D. 2017, *ApJ*, 838, 41
- Kaspi, S., Smith, P. S., Netzer, H., et al. 2000, *ApJ*, 533, 631
- Larkin, J., et al. 2006, *Proc. SPIE*, 6269, 42
- Leighly, K. M. 2004, *ApJ*, 611, 125
- Markwardt, C. B. 2009, *Astronomical Data Analysis Software and Systems XVIII*, 411, 251
- Marton, G., Calzoletti, L., Perez Garcia, A. M., et al. 2017, *arXiv:1705.05693*
- Marziani, P., Sulentic, J. W., Plauchu-Frayn, I., & del Olmo, A. 2013, *A&A*, 555, A89
- Mazzucchelli, C., Bañados, E., Venemans, B. P., et al. 2017, *ApJ*, 849, 91
- McLure, R. J., & Jarvis, M. J. 2002, *MNRAS*, 337, 109
- McLure, R. J., & Dunlop, J. S. 2004, *MNRAS*, 352, 1390
- Mejía-Restrepo, J. E., Trakhtenbrot, B., Lira, P., Netzer, H., & Capellupo, D. M. 2016, *MNRAS*, 460, 187
- Melbourne, J., Peng, C. Y., Soifer, B. T., et al. 2011, *AJ*, 141, 141
- Melbourne, J., Soifer, B. T., Desai, V., et al. 2012, *AJ*, 143, 125
- Mineshige, S., Kawaguchi, T., Takeuchi, M., & Hayashida, K. 2000, *PASJ*, 52, 499
- Murray, N., & Chiang, J. 1997, *ApJ*, 474, 91
- Netzer, H., Lira, P., Trakhtenbrot, B., Shemmer, O., & Cury, I. 2007, *ApJ*, 671, 1256
- Oke, J. B., Cohen, J. G., Carr, M., et al. 1995, *PASP*, 107, 375
- Onken, C. A., & Kollmeier, J. A. 2008, *ApJ*, 689, L13
- Park, D., Barth, A. J., Woo, J.-H., et al. 2017, *ApJ*, 839, 93
- Polletta, M., Tajer, M., Maraschi, L., et al. 2007, *ApJ*, 663, 81
- Peterson, B. M. 1993, *PASP*, 105, 247
- Ricci, C., Assef, R. J., Stern, D., et al. 2017, *ApJ*, 835, 105
- Richards, G. T., Vanden Berk, D. E., Reichard, T. A., et al. 2002, *AJ*, 124, 1
- Richards, G. T., Lacy, M., Storrie-Lombardi, L. J., et al. 2006, *ApJS*, 166, 470
- Roche, P. F., Aitken, D. K., Smith, C. H., & James, S. D. 1986, *MNRAS*, 218, 19P
- Runnoe, J. C., Brotherton, M. S., Shang, Z., & DiPompeo, M. A. 2013, *MNRAS*, 434, 848
- Schulz, B., Marton, G., Valtchanov, I., et al. 2017, *arXiv:1706.00448*
- Shen, Y., Greene, J. E., Strauss, M. A., Richards, G. T., & Schneider, D. P. 2008, *ApJ*, 680, 169-190
- Shen, Y., Richards, G. T., Strauss, M. A., et al. 2011, *ApJS*, 194, 45
- Silva, L., Granato, G. L., Bressan, A., & Danese, L. 1998, *ApJ*, 509, 103
- Skrutskie, M. F., Cutri, R. M., Stiening, R., et al. 2006, *AJ*, 131, 1163
- Spoon, H. W. W., Keane, J. V., Tielens, A. G. G. M., Lutz, D., & Moorwood, A. F. M. 2001, *A&A*, 365, L353
- Spoon, H. W. W., Marshall, J. A., Houck, J. R., et al. 2007, *ApJ*, 654, L49
- Suh, H., Hasinger, G., Steinhardt, C., Silverman, J. D., & Schramm, M. 2015, *ApJ*, 815, 129
- Sulentic, J. W., Bachev, R., Marziani, P., Negrete, C. A., & Dultzin, D. 2007, *ApJ*, 666, 757
- Trakhtenbrot, B., Netzer, H., Lira, P., & Shemmer, O. 2011, *ApJ*, 730, 7
- Trakhtenbrot, B., & Netzer, H. 2012, *MNRAS*, 427, 3081
- Tsai, C.-W., Eisenhardt, P. R. M., Wu, J., et al. 2015, *ApJ*, 805, 90
- Tsai, C.-W., et al. in preparation
- Tsuzuki, Y., Kawara, K., Yoshii, Y., et al. 2006, *ApJ*, 650, 57
- Vega, O., Clemens, M. S., Bressan, A., et al. 2008, *A&A*, 484, 631
- Vestergaard, M. 2002, *ApJ*, 571, 733
- Vestergaard, M., & Peterson, B. M. 2006, *ApJ*, 641, 689
- Vestergaard, M., & Wilkes, B. J. 2001, *ApJS*, 134, 1
- Vito, F., Brandt, W. N., Eisenhardt, P. R., et al. 2017, *MNRAS*, in press
- Wandel, A., Peterson, B. M., & Malkan, M. A. 1999, *ApJ*, 526, 579
- Wang, J.-G., Dong, X.-B., Wang, T.-G., et al. 2009, *ApJ*, 707, 1334
- Wang, R., Carilli, C. L., Neri, R., et al. 2010, *ApJ*, 714, 699
- Wang, J.-M., & Zhou, Y.-Y. 1999, *ApJ*, 516, 420
- Watarai, K.-y., Fukue, J., Takeuchi, M., & Mineshige, S. 2000, *PASJ*, 52, 133
- Wright, E. L., Eisenhardt, P. R. M., Mainzer, A. K., et al. 2010, *AJ*, 140, 1868
- Wu, J., Tsai, C.-W., Sayers, J., et al. 2012, *ApJ*, 756, 96
- Wu, X.-B., Wang, F., Fan, X., et al. 2015, *Nature*, 518, 512
- Wu, J., Jun, H. D., Assef, R. J., et al. 2018, *ApJ*, 852, 96